Physics of Plasmas ARTICLE pubs.aip.org/aip/pop

Prepulse-induced changes in ion acceleration direction: Insights from TNSA regime experiments and simulations at PHELIX

Cite as: Phys. Plasmas **32**, 083105 (2025); doi: 10.1063/5.0278103
Submitted: 28 April 2025 · Accepted: 30 July 2025 ·
Published Online: 19 August 2025

P. Boller,[1,2,3,a)] J. Hornung,[1] A. Dumitru,[4,5] C. Kanstein,[1,2] E. Oezalp,[1,2] J. B. Ohland,[1,6] L. Wegert,[1] and V. Bagnoud[1,2,3,7]

AFFILIATIONS

[1]GSI Helmholtzzentrum für Schwerionenforschung GmbH, Planckstr. 1, 64291 Darmstadt, Germany
[2]Institute for Applied Physics, Technical University Darmstadt, Hochschulstraße 6, 64289 Darmstadt, Germany
[3]Helmholtz Forschungsakademie Hessen für FAIR, Schlossgartenstr. 2, 64289 Darmstadt, Germany
[4]Extreme Light Infrastructure - Nuclear Physics, Strada Reactorului 30, Măgurele 077125, Romania
[5]National University of Science and Technology POLITEHNICA Bucharest, Splaiul Independentei 313, 060042 Bucharest, Romania
[6]Laboratoire pour l'Utilisation des Lasers Intenses, Ave. Fresnel, 91120 Palaiseau, France
[7]Helmholtz Institute Jena, Max Wien Platz 1, 07745 Jena, Germany

[a)]Author to whom correspondence should be addressed: p.boller@gsi.de

ABSTRACT

We present an experimental and simulation-based study on ion beam deflection in laser-matter interactions conducted at the PHELIX facility. The experiment was performed using a main pulse (1053 nm, 500 fs) reaching peak intensities of $\sim 1.5 \times 10^{21}$ W cm^{-2}, and a pre-pulse (1053 nm, either 1 or 3 ns) with an intensity ranging from 6.4×10^{13} to 1.2×10^{15} W cm^{-2}. The laser was incident on a 5 μm thick carbon foil under an angle of 25° relative to the target normal. Systematic variation of the pre-pulse delay (0–3 ns) revealed significant target deformation effects, leading to ion beam deflection and a reduction of the ion cutoff energies with increasing delay between the pre-pulse and the main pulse. The pre-plasma dynamics were characterized using side-view interferometry in combination with a synchronized picosecond probe beam. Hydrodynamic simulations with FLASH-2D were adapted to match the interferometric measurements by adjusting laser energy and focus size. The simulations confirm that the observed beam deflection originates from pre-pulse-induced target deformation and expansion. Our results demonstrate that ion beam directionality can be controlled via pre-pulse parameters, providing a pathway for optimizing laser-driven ion acceleration schemes. These findings highlight the importance of precisely adapted pre-plasma conditions in high-intensity laser-plasma interactions and their impact on acceleration dynamics.

I. INTRODUCTION

Advances in ultrahigh-intensity laser technology have established laser-driven ion acceleration as a promising field of research, motivated by the prospects of harnessing its unique properties for scientific and practical applications.[1–4] Compared to conventional accelerator facilities, laser-driven ion sources could provide a compact and cost-efficient alternative. They deliver ion beams with exceptionally high brightness, low beam emittance, and ultrashort pulse duration,[2,5–7] making them promising candidates for applications in medicine, materials science, and next-generation accelerator technologies.[8–11]

Recent experiments on laser-ion acceleration have demonstrated proton beams with cutoff energies exceeding 150 MeV by optimization of target thickness and the use of advanced acceleration schemes.[12–14] Among the various acceleration mechanisms, Target Normal Sheath Acceleration (TNSA) remains one of the most robust and widely studied mechanisms.[15–18] In TNSA, electrons accelerated by an intense laser pulse establish a sheath field at the rear surface of a thin solid target, leading to ion acceleration in the target normal direction. However, the presence of pre-plasma, generated by amplified spontaneous emission (ASE) or pre-pulses, significantly modifies the conditions for ion acceleration.[19]

Pre-plasma expansion leads to multiple effects that influence laser-plasma interaction and ion acceleration in contradictive ways. A moderate pre-plasma can enhance laser absorption and improve electron heating, strengthening the sheath field at the target rear side.[20] However, excessive pre-plasma formation can drastically modify the interaction. A shock wave generated at the target front surface propagates through the material, leading to significant deformation or even destruction of thin foils before the main pulse arrives.[19,21] This deformation alters the sheath field topology and shifts the effective acceleration direction. Additionally, expansion at the target rear side lowers the accelerating field strength, reducing maximum ion energies. Further effects include whole-target displacement, which can change the laser intensity distribution seen by the target, thereby modifying the acceleration process. In addition, these intricate effects are hard to measure and simulate because of the time and intensity scales on which they take place.

Previous studies, using the naturally present ASE pedestal of the laser, have extensively investigated the impact of pre-plasma on laser-ion acceleration. Batani *et al.* demonstrated that pre-plasma formation alters the energy distribution of accelerated ions and systematically shifts the ion beam direction away from the target normal toward the laser propagation axis.[19] Zheng *et al.* used particle-in-cell (PIC) simulations to investigate how optimized pre-plasma conditions can improve ion beam properties by modifying electron heating and sheath dynamics.[22] Similarly, Hadjisolomou *et al.* used both hydodynamic and PIC simulations to analyze pre-plasma effects on ion acceleration,[23] while Yogo *et al.* investigated pre-plasma-induced target deformation.[24] Flacco *et al.* performed experimental and numerical studies on controlled plasma expansion, providing a detailed characterization of pre-plasma evolution in vacuum and its implications for laser-ion acceleration.[25]

While these studies have provided valuable insights into the effects of pre-plasma on ion energy spectra, they often focus on energy distributions. In addition, the laser pre-pulse resulting from the ASE of the laser offers little control possibilities. A key challenge that remains insufficiently addressed is the precise control of ion beam directionality in the presence of a modifiable pre-plasma. The ability to steer ion beams via controlled target deformation could provide new opportunities for optimizing laser-driven ion acceleration setups.

In this work, we present a systematic experimental and simulation-based study on the influence of pre-plasma on ion beam deflection and proton cutoff energy in the TNSA regime, using an independently tunable pre-pulse. The experiment was conducted at the PHELIX facility[26] at GSI Helmholtzzentrum für Schwerionenforschung in Darmstadt, Germany, where the pre-plasma conditions were systematically varied by introducing a controlled pre-pulse of variable delay and pulse duration. The pre-plasma dynamics were monitored using side-view interferometry with a synchronized probe beam laser. The experimental observations were compared to hydrodynamic simulations performed with FLASH-two-dimensional (2D),[27] which were adapted to match the interferometric measurements by adjusting laser energy and beam focus.

Our results demonstrate that pre-pulse-induced target deformation not only affects ion energy spectra but also leads to a systematic deflection of the ion beam away from the initial target normal direction. By validating our simulations against experimental interferometric data, we demonstrate the capability to model pre-plasma dynamics in high-intensity laser interactions. These findings provide new insights into the role of pre-plasma parameters in ion beam steering, which could be leveraged for improved control in future laser-ion acceleration experiments.

Section II introduces the experimental setup and diagnostics used in the campaign. The analysis of the interferometric data are detailed in Sec. III. In Sec. IV, hydrodynamic simulations with FLASH-2D are presented and compared to the experimental measurements. Afterwards, Sec. V discusses the results of the ion diagnostics. Section VI concludes the paper with a summary and discussion.

II. EXPERIMENTAL SETUP

The presented experiment was conducted at the PHELIX facility at GSI Helmholtzzentrum für Schwerionenforschung in Darmstadt, Germany.[26] Figure 1 provides a schematic of the experimental setup.

The front end of PHELIX comprises two independent laser sources operating at the central wavelength of 1053 nm, which are combined before the pre-amplifier. Whereas the femtosecond front end delivers ultrahigh-temporal-contrast pulses used as the main TNSA driver pulse, the nanosecond front end produces narrowband pulses synchronized with the main pulse, which are used as the pre-pulse. This configuration ensures that both pulses share the same beam path and pointing, and the pre-pulse can be precisely tuned in delay and amplitude, allowing for comparative studies with and without enhanced pre-plasma formation. The ASE level of the main pulse was characterized prior to the experimental campaign and remained below 10^{12} W cm^{-2} more than 80 ps before the main pulse, and its influence is negligible compared to the controlled pre-pulse introduced in this study.

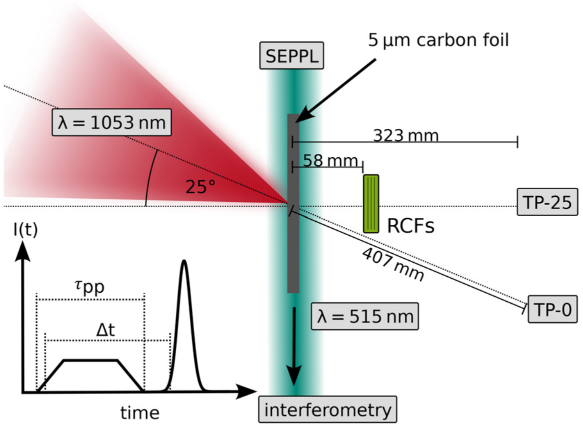

FIG. 1. Schematic sketch of the experimental setup at PHELIX. The laser delivers a pre-pulse with a pulse duration of τ_{PP} and a delay Δt relative to the main pulse, which is focused onto the target. The timing diagram illustrates the definition of Δt as the time between the rising edges of both pulses, which result in temporal overlap for short delays. For pre-plasma characterization, the Seeded Experimental Plasma Probe Laser (SEPPL) is used as an interferometric setup. Behind the target, an RCF stack and two Thomson parabola spectrometers (TP-0 and TP-25) are positioned at defined angles relative to the laser axis.

To characterize the focal spot of both beams, spatial intensity profiles were recorded during alignment prior to each laser shot using the unamplified laser pulses. From these images, two metrics were extracted: the full width at half maximum (FWHM) of a simple Gaussian fit to the radial profile, and the radius enclosing 50% of the total energy, obtained via direct integration of the 2D intensity map. The main pulse was tightly focused to a FWHM of $2.66 \pm 0.13\ \mu$m and a half-energy radius of $2.32 \pm 0.33\ \mu$m. The quoted uncertainties represent the standard deviation across all evaluated shots. To achieve a more uniform preheating of the target, the pre-pulse beam was designed to be smaller in the near field. This resulted in a focal spot with a FWHM of $8.12 \pm 0.11\ \mu$m and a half-energy radius of $5.01 \pm 0.23\ \mu$m. Again, the uncertainties reflect the standard deviation observed over multiple shots. A programmable arbitrary waveform generator was used to generate a trapezoidal temporal shape for the pre-pulse, with rise and fall times of 250 ps, resulting in a total pre-pulse duration τ_{pp} of either 1 or 3 ns. The 1 ns setting was used most frequently, while the extended pre-pulse duration of 3 ns helped to minimize relative timing uncertainties with respect to the main pulse.

The temporal delay Δt between the pre- and main pulse was defined as the time interval between the points at which both pulses reached 10% of their respective peak intensities during the rising edge. To calibrate the electronically adjusted delay settings, unamplified leak signals of both pulses were simultaneously recorded using a fast photodiode placed at the main amplifier and recorded with a Tektronix MSO64 oscilloscope (4 GHz bandwidth, 2.5 GS/s). Since both pulses were visible on the same trace, their relative delay Δt could be extracted from the temporal distance between the two pulse peaks. A linear fit to the measured values yielded the calibration curve. Shot-to-shot fluctuations introduced a total timing uncertainty of 0.3 ns (peak-to-valley). The delay Δt in our experimental campaign was systematically varied from 0.3 to 3 ns to study its effect on target expansion and ion acceleration. For short delay times, the main pulse overlaps with the pre-pulse.

The energy of both pulses varied due to shot-to-shot fluctuations, and was measured before the compressor with a transmission efficiency of 81%. However, the ns pre-pulse energy remained relatively stable, resulting in mean energy on target of 0.81 ± 0.05 J. In contrast, the fs main pulse energy fluctuated more strongly, ranging from 81–122 J on target. Laser focus optimization for maximum intensity was achieved using a deformable mirror in combination with an absolute wavefront calibration routine, as described by Ohland *et al.*[28]

Several carbon foils, each $5\ \mu$m thick and produced via sputter deposition by GSI's Target Laboratory,[29] were implemented in the experimental campaign. Each foil was mounted on the facility's standard motorized 4-axis positioning system and aligned at an incidence angle of 25° with respect to the laser axis. The s-polarized laser pulse was focused onto the target using a diamond-turned F/1.7 off-axis copper parabola.

The on-target laser intensity was estimated using the recorded focus images during alignment as mentioned earlier and the typical PHELIX pulse duration[18] for the main pulse and the configured pulse length for the pre-pulse. Because PHELIX features an active beam correction that minimizes the on-shot beam distortion, we believe this method delivers a high-fidelity estimate of the on-shot focus intensity. For the main pulse with a duration of 500 ± 50 fs, the mean peak intensity is estimated to be $1.47(30) \times 10^{21}\ \mathrm{W\,cm^{-2}}$, where the uncertainty corresponds to the standard deviation across all analyzed shots. The pre-pulse intensity, in contrast, was significantly lower, and ranged between 6.4×10^{13} and $1.2 \times 10^{15}\ \mathrm{W\,cm^{-2}}$, depending on the individual shot. For delays of a few hundred picoseconds, the resulting pre-pulse situation is quite unique, while for longer durations above 1 ns, it emulates the ASE temporal plateau found in standard chirped pulse amplification (CPA) laser systems.

To characterize the pre-plasma formation, we used a probe beam from the in-house-developed, frequency-doubled off-harmonic Seeded Experimental Plasma Probe Laser (SEPPL).[30] This laser operates at a central wavelength of 515 nm and its pulse length was set to 2.5 ps for the experiment, allowing for quasi-instantaneous snapshots of the pre-plasma evolution on sub-nanosecond timescales. The probe beam transmitted through the pre-plasma accumulated a phase delay due to variations in the electron density and thus the refractive index. A Mach–Zehnder interferometer with a 16-bit camera overlapped the part of the beam passing through the plasma with an unperturbed part and captured the resulting fringe pattern, from which the phase shift was directly extracted. Assuming cylindrical symmetry, the electron density distribution was reconstructed via inverse Abel transform (see Sec. III).

The accelerated ion beam was characterized using a stack of radiochromic films (RCFs) and two Thomson parabola (TP) spectrometers, the relative position of which can be seen in Fig. 1. The RCFs, measuring $50 \times 50\ \mathrm{mm}^2$, included HD-V2 and EBT3 Gafchromic films, each containing a 3 mm wide slit to allow ion detection by the Thomson parabola spectrometers. The front surface of the RCF stack was positioned 58 mm from the target to measure the spatially resolved ion energy distributions. Due to the geometrical setup, the RCFs did not capture ions emitted exactly along the laser axis. The first film layer covered an angular range from 1.7° to 48.3° with respect to the laser axis. The TP spectrometers enabled energy and charge state measurements of the accelerated ions by deflecting them through crossed electric and magnetic fields before reaching an imaging plate. They were positioned at distances of 407 mm (TP-0) at 0° and 344 mm (TP-25) at 25° relative to the laser axis. TP-0 has a conventional design with parallel electrostatic plates, ensuring a homogeneous field of ~1.11 MV/m from a 10 kV potential difference across 9 mm. The magnetic field strength was 1.01 T, extending over 100 mm. In contrast, TP-25 utilized an adapted electrostatic design with non-parallel plates.[31] The plate separation increased from 2.39 mm at the entrance to 22.5 mm at the exit, resulting in a position-dependent electric field. A voltage of 4 kV was applied across the plates. The magnetic field extended over 70 mm, with a peak strength of 0.597 T and an average field of 0.373 T, providing ion deflection for species separation. Both spectrometers featured a $100\ \mu$m diameter pinhole, which defined the angular acceptance and spatial resolution of the detected ion beam. The calculated acceptance angles were 0.122 mrad for TP-0 and 0.140 mrad for TP-25, respectively, determining the maximum divergence of ions reaching the detector.

This setup of diagnostics ensured precise characterization of the laser–plasma interactions and facilitated a detailed analysis of the resulting phenomena.

III. ANALYSIS OF INTERFEROMETRIC DATA

Optical interferometry is a well-established diagnostic method in laser-plasma physics to measure the electron density of an undercritical plasma.[32,33] A probe beam passing through the plasma accumulates a phase shift due to changes in the electron density and thus the refractive index. By recording interference fringes, the phase shift can be extracted and converted into spatially resolved electron density maps, assuming a cylindrical geometry. In this section, we present the analysis of the interferometric data, detailing the image acquisition, phase extraction, and electron density reconstruction.

The interferometric setup utilized the in-house developed SEPPL operating at a central wavelength of 515 nm and a pulse length of 2.5 ps.[30] To ensure synchronization, the probe laser was temporally shifted such that its rising edge overlapped with the rising edge of the main pulse in the interaction point. Given the pulse duration of SEPPL, the interaction geometry of the interferometry setup and plasma dimensions, we assume a precision in the relative timing between the interformetry and driver pulse at a few picoseconds, which is small compared to plasma expansion dynamics before the main pulse. For each laser shot, an interferometric image was recorded to take a snapshot of the pre-plasma expansion just before the interaction with the main pulse. In addition to the on-shot image, a background image and a reference image were taken before the laser interaction. After passing the expanded plasma from the target, the probe beam was directed through a Mach–Zehnder interferometer, which overlapped the part of the beam that passed through the plasma with an unperturbed part. A 16-bit camera recorded high-spatial-resolution interference fringes, which remain well resolved without saturation. Figure 2 shows an example of a reference and on-shot image. The main laser pulse is coming from the left side. In the reference picture, the target shadow is visible in the darker area. The target foil is slightly curved. In the on-shot picture, two features become visible: first, a shadow of the plasma around the interaction region is visible. This effect is due to the deflection of the probe laser rays in areas of strong plasma density gradients and limits the electron density region accessible via interferometry. Second, the interference pattern is visibly different from the reference picture and it encodes the plasma density information. The red curve indicates the region, where a reconstruction of the electron density is not possible.

To extract the phase shift $\delta\phi$ from the interferometric images, a Fast Fourier Transform (FFT) method was applied. The first-order spatial frequency component, which carries the phase information, was isolated from both the reference and on-shot images using a Gaussian filter. An inverse FFT followed by subtracting the reference from the on-shot image yielded the spatial phase distribution. The resulting phase shift, denoted as $\delta\phi(x, y)$, was then unwrapped to isolate the plasma-induced contribution.

The relation between the phase shift accumulated along the propagation in the plasma and the index of refraction n_0 is given by

$$\delta\phi(x,y) = \frac{2\pi}{\lambda}\int_z \left(n_0(x,y,z) - 1\right) dz, \tag{1}$$

where λ is the probe laser wavelength. Being able to retrieve the index of refraction information will lead to the electron density $n_e(z)$, where index of refraction and free electron density in the plasma are linked by

$$n_e(x,y,z) = \left(n_0^2(x,y,z) - 1\right) n_c, \tag{2}$$

$$n_c = \frac{\epsilon_0 m_e \omega^2}{e^2}, \tag{3}$$

where n_c is the critical electron density defined as function of ϵ_0 the permittivity of free space, m_e the electron mass, ω the angular frequency of the probe laser, and e the elementary charge.

Direct inverting of Eq. (1) is not possible without additional assumptions. However, when assuming a cylindrical symmetry, i.e., $n_0(x,y,z) = n_0(x,r)$ with $r = \sqrt{y^2 + z^2}$, it is possible to invert the problem using the Abel inversion and find $n_0(x,r)$. Here, critical parameters are the position of the axis at $r = 0$, and the necessity to start with symmetrical plasma images.

The final reconstructed electron density distribution is shown on logarithmic scale in Fig. 3. White regions mark areas of low electron density not resolved by the interferometer dynamic range (negative values), as well as regions within the target shadow with high electron density and/or high electron density gradients. The red curve indicates the boundary beyond which electron density reconstruction is no

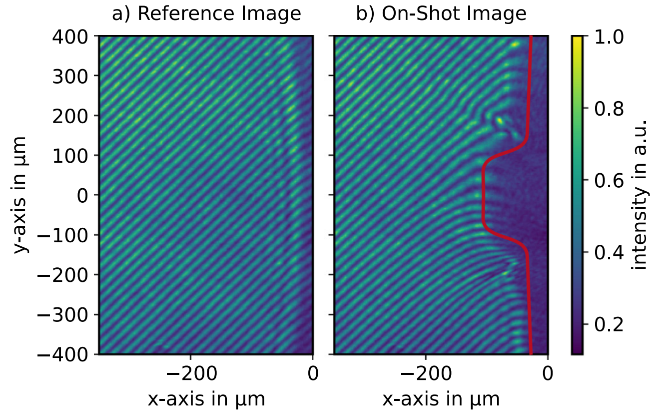

FIG. 2. (a) Reference interferometric image and (b) on-shot interferometric image at the time of the main pulse arrival. The darker area without fringes represents the high-density region above 3×10^{19} cm^{-3}, corresponding to (a) the target before laser interaction and (b) the expanded plasma. In this region, the probe laser could not penetrate the plasma or was significantly deflected due to steep electron density gradients. The red curve marks the boundary above which no reliable electron density reconstruction is possible.

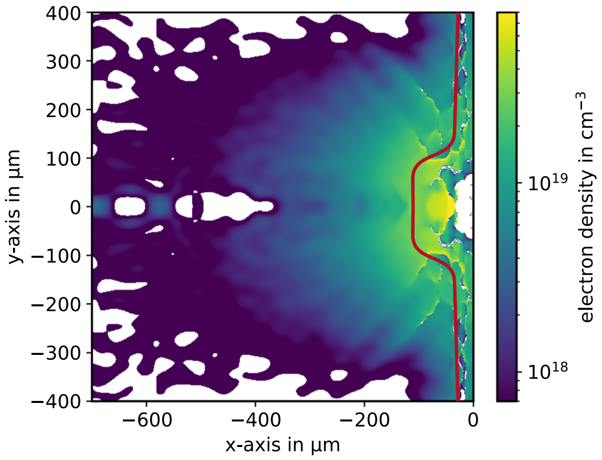

FIG. 3. Reconstructed 2D electron density distribution from the interferometric image. The white regions correspond to areas outside the reconstructed dynamic range. The red curve indicates the region above which a meaningful electron density reconstruction is not feasible.

longer feasible. A noise level on the order of $\sim 10^{18}$ cm^{-3} was estimated by comparing two reference images (without plasma) from two different laser shots. Given a maximum electron density of 3×10^{19} cm^{-3}, this corresponds to a dynamic range of $\sim$30.

This interferometric analysis provides key insights into the pre-plasma expansion dynamics, enabling direct comparisons with hydrodynamic simulations (see Sec. IV).

IV. HYDRODYNAMIC SIMULATIONS WITH FLASH-2D AND COMPARISON WITH INTERFEROMETRY DATA

For experiments involving ultrahigh laser intensities, the intensity required to start ionizing the target material is usually reached long before the interaction conditions enter the relativistic regime. As a consequence, the plasma begins to expand hydrodynamically during the early stages of the interaction. In our experiment, this behavior was emulated by introducing an artificial pre-pulse, which allows for controlled studies of pre-plasma formation prior to the arrival of the main pulse.

Hydrodynamic simulation tools can be used to describe this effect, providing detailed insights into plasma evolution, particularly in regimes where experimental diagnostics are limited.[34–37] The goal of the simulations presented in this section is to model the evolution of the pre-plasma and to reproduce the experimentally observed density distributions at the time of main pulse arrival. For this purpose, the FLASH-2D code,[27] an adaptive-mesh radiation hydrodynamics solver was employed.

Generally, hydrodynamic simulations typically rely on equation-of-state models that assume local thermodynamic equilibrium. However, laser-plasma interaction experiments involving ultrashort laser pulses can exhibit highly transient, non-equilibrium behavior in both space and time, which introduces uncertainties in the simulation outcome. Therefore, key input parameters such as the pre-pulse energy and beam waist were systematically varied and benchmarked against the interferometric measurements to ensure realistic modeling of the pre-plasma conditions.

To approximate the experimental conditions while maintaining computational efficiency, a cylindrical 2D geometry with normal laser incidence (0°) was employed in the simulations. This differs from the experimental setup, where the laser was incident at an angle of 25° with respect to the target normal. The choice of normal incidence is justified by the predominantly target-normal plasma expansion dynamics. This was also confirmed by an additional three-dimensional (3D) Cartesian simulation, including the actual angle of incidence. Apart from this geometric simplification, all other parameters were chosen to closely reproduce the experimental conditions (see Fig. 1). The 5 μm thick target was initialized at a temperature of 290 K. The material was modeled as graphite using the SESAME equation of state (EOS) table 7832.[38] Opacity values were generated using the Transport Opacity Processing System (TOPS) multigroup opacity code,[39] with six spectral groups applied in the simulations. The laser pre-pulse was modeled with 250 ps rise and fall times and a constant intensity plateau. A focal spot size of 8.55 μm (FWHM) and a laser energy of 1 J was used in the simulations, slightly larger than the experimentally measured value of 8.12 ± 0.11 μm and 0.81 ± 0.05 J.

Several physical effects are visible in the simulation results. In addition to plasma formation at the front side of the target, a shock wave is generated at the beginning of the simulation, propagating through the target and leading to the disruption of the thin foil. Furthermore, a complete target displacement is observed in the density profiles.

To adjust the simulations to the interferometric data, the laser energy and beam waist were systematically varied. The interferometry probed the plasma after a 3 ns pre-pulse (without main pulse), and the simulations were performed for the same duration to match the measurement time. Using the long pre-pulse of 3 ns minimizes the influence of the relative timing jitter between the interferometry laser and the pre-pulse, as the fixed jitter of 0.3 ns (peak-to-valley) represents only a small fraction of the total pre-pulse duration.

In one set of simulations, the laser intensity was kept constant by scaling the beam waist with the square root of the energy, isolating the effect of different energy input [Fig. 4(a)]. In another set, only the laser

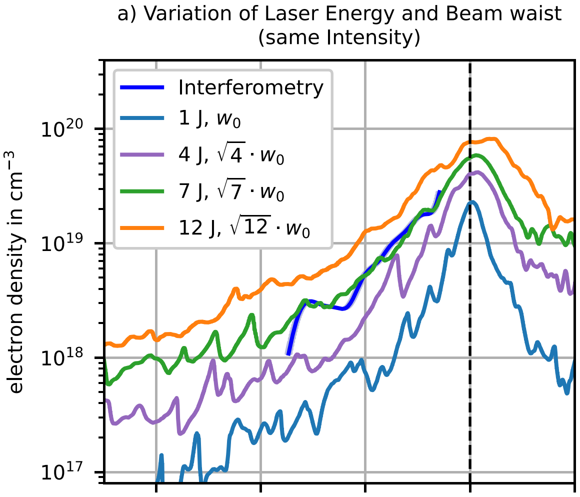

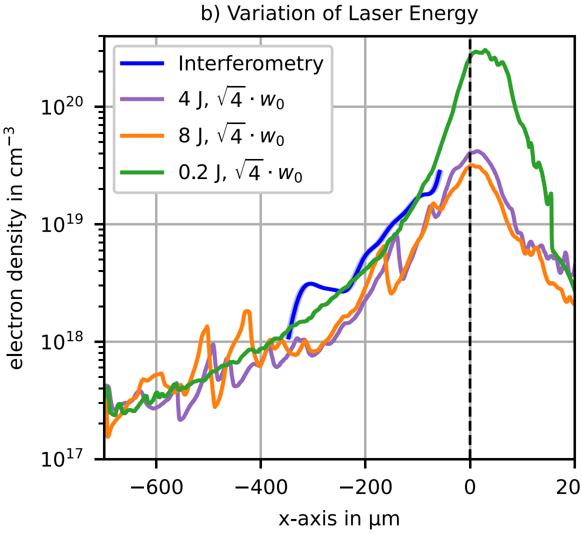

FIG. 4. Comparison of interferometry data and simulated electron density lineouts along the laser propagation axis at the center ($y = 0 \mu$m) after a 3 ns pre-pulse. In (a), the laser energy and beam waist were varied while keeping the intensity constant. In (b), only the laser energy was varied. The black dashed line represents the initial front surface of the target, which extends from $x = 0$ to $x = 5\mu$m.

energy was varied while maintaining a fixed beam waist, enabling an analysis of the influence of different on-target intensities [Fig. 4(b)]. Figure 4 shows the electron density lineout along the laser axis after a pre-pulse of $t_{\mathrm{PP}} = 3\mathrm{ns}$. Using the experimental data as input to the simulation leads to plasma densities that underestimates the experimental data measured by interferometry. The input parameters to the simulation were then manually adjusted to improve the agreement between simulations and experiments. The comparison of the experimental and simulated electron density profiles shows that the simulation with a laser energy of 7 J and a beam waist scaled by a factor of $\sqrt{7}$, corresponding to a constant laser intensity, matches best with the interferometric data, both in terms of density gradient and absolute electron density values in the central region where the main laser interaction occurs.

When only the laser energy is varied with a fixed beam waist, density modifications occur mainly in the region of the initial target position, while the density distribution in the pre-plasma remains nearly unchanged. Simulations with higher laser energy indicate a faster temporal evolution of the plasma expansion, leading to a more rapid depletion of the target material. These results highlight the importance of adjusting both the laser energy and the beam waist to accurately reproduce the experimentally observed electron density profiles, while keeping the on-target intensity constant.

The modified simulation parameters, with an increased laser energy of 7 J instead of 1 J and an adjusted beam waist of $\sqrt{7}$, ensuring constant laser intensity, were also applied to a pre-pulse duration of $\tau_{\mathrm{PP}} = 1\mathrm{ns}$ with varying delays Δt. Figure 5 shows the electron density lineouts along the laser propagation axis at the center ($y = 0\mu\mathrm{m}$) for delays of 0.5 and 1.5 ns. At smaller delays compared to the 3 ns, the target remains opaque, as indicated by the critical density threshold. The simulations show good agreement with the interferometric data in the low-density region for various delays.

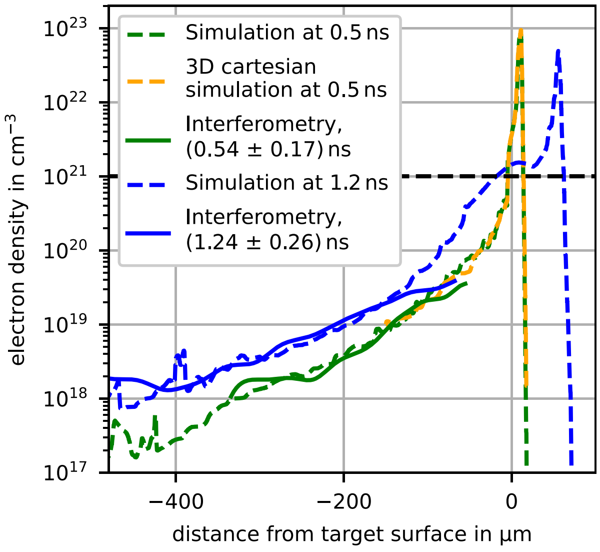

FIG. 5. Comparison of interferometry data and simulated electron density lineouts along the laser propagation axis at the center ($y = 0\mu\mathrm{m}$) with a pre-pulse duration of 1 ns and varying pulse delays. A 3D simulation was added for comparison. The black dotted line represents the critical density, indicating that the target remains opaque in these cases.

While the primary analysis was based on two-dimensional (2D) cylindrical simulations, three-dimensional (3D) simulations were performed for comparison. Due to computational constraints, these were carried out with a smaller simulation box and only for short delay times Δt. The results confirm that the 2D cylindrical approximation accurately reproduces the plasma expansion dynamics observed in 3D simulations, as evidenced by the agreement in the electron density lineouts. Additionally, the 3D results support the assumption that the dominant plasma expansion during the pre-pulse occurs primarily in the target-normal direction.

The simulation results closely reproduce the pre-plasma expansion observed in the interferometric measurements, indicating that the adapted FLASH-2D simulation provides a good representation of the laser-matter interaction during the pre-pulse phase.

V. LASER-ION ACCELERATION

This section presents the experimental results on laser-ion acceleration and their dependence on the pre-pulse parameters. The accelerated ions were diagnosed using two TP spectrometers positioned at 0° (TP-0) and 25° (TP-25) relative to the laser axis, and a stack of RCFs (see Fig. 1).

Figure 6 presents the measured proton cutoff energy normalized by the square root of the applied laser energy for different pre-pulse delays Δt. The choice of normalization is motivated by previous experimental findings, where a scaling with the laser peak power, as proposed by Zeil *et al.*,[40] showed better agreement with measured data than a scaling with on-target intensity. This behavior was observed in earlier experiments at PHELIX, where the laser power scaling reproduced the observed trends more reliably.[18] While alternative empirical scalings exist, such as the one proposed by Zimmer *et al.*,[41] the square root normalization was chosen here for consistency and simplicity. In

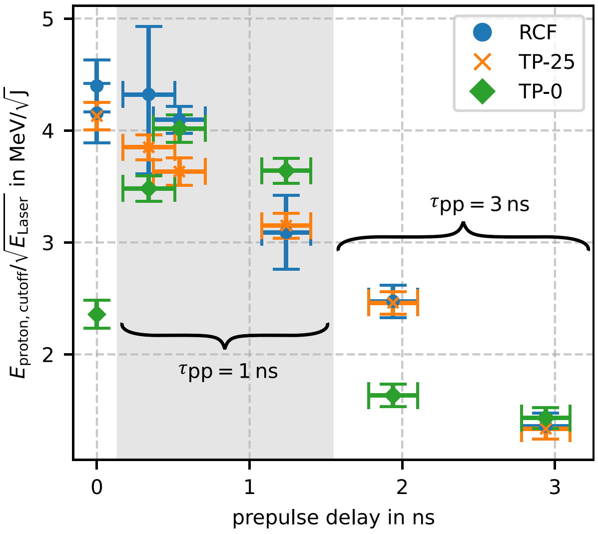

FIG. 6. Measured proton cutoff energy, recorded with RCFs, TP-25 (target normal direction), and TP-0 (laser direction), normalized by the square root of the applied laser energy as a function of pre-pulse delay Δt. The shaded area corresponds to shots with a pre-pulse duration $\tau_{\mathrm{PP}} = 1\,\mathrm{ns}$, while the others used $\tau_{\mathrm{PP}} = 3\,\mathrm{ns}$. The data points at $\Delta t = 0$ corresponds to a laser shot without an additional induced pre-pulse.

our case, the assumption of Target Normal Sheath Acceleration (TNSA) as the dominant mechanism is justified by the use of relatively thick targets and further supported by transmitted light measurements (not shown in the experimental setup for simplicity), which were performed using a calorimeter. These measurements confirmed that the targets remained opaque during the interaction, excluding significant contributions from alternative acceleration mechanisms.

In addition to a laser shot without an induced pre-pulse, the experiment included two different pre-pulse durations of 1 and 3 ns, each delivering $\sim$1 J of energy. Only the relative delay between the pre- and main pulses was varied across the scan. In Fig. 6, the data points at $\Delta t = 0$ns represents the laser shot without an explicit pre-pulse.

The data in Fig. 6 reveal a systematic decrease in proton cutoff energy with increasing pre-pulse delay. This trend is observed in both the RCF and TP data, which show good overall agreement. We attribute this to target rear-side expansion, and a subsequent decrease in the accelerating sheath field strength. In the absence of a pre-pulse (corresponds to values with 0 ns delay), ion acceleration follows the classic TNSA mechanism, with the highest proton energies observed in the target normal direction (TP-25). In contrast, with increasing pre-pulse delay, the ion beam progressively shifts toward the laser propagation direction, as detected by TP-0. For longer pre-pulse durations and delays, this directional shift is not observed, and the overall proton cutoff energies appear significantly reduced.

This shift in acceleration direction is further confirmed by RCF measurements, which provide spatial information about the ion beam profile. Figure 7 displays RCFs of the last layer for each shot, showing the highest measured proton energy. While the case without a pre-pulse is the classic TNSA case, one clearly sees the deflection for the cases with increasing pre-pulse delay. For the longer pre-pulses, artifacts are visible indicating a destruction of the target by the arrival of the main pulse.

All relevant laser parameters, focal spot sizes, and extracted scale lengths for each shot are summarized in Table I. The scale lengths L_n were obtained at an electron density of $n_e = 10^{19}\text{cm}^{-3}$, both from experimental interferometric reconstructions and from hydrodynamic simulations. For the shot without a pre-pulse, no measurable expansion occurred, and the experimental reconstruction could not resolve the density gradient. In this case, a simulated scale length based on the rising slope of the laser envelope is provided.

In general, we observe reasonable agreement between measured and simulated values, with overlapping 3σ error bars for all shots except for the one at $\Delta t = 0.34$ns. For short delays, the interferometric reconstruction is challenged by diffraction effects and limited resolution, as the resulting pre-plasma is compact and the fringe shifts are confined to a narrow region near the target surface.

While the pre-plasma scale length is a critical parameter for characterizing the interaction conditions, especially in the context of laser energy absorption and ion acceleration mechanisms, it should be noted that our interferometric diagnostic does not resolve densities near or above the critical density n_c. Thus, the extracted scale lengths reflect the conditions in the underdense region. Nevertheless, it has been shown that the scale length at or near the critical density plays a central role in determining the efficiency and scaling behavior of TNSA acceleration.[42]

We attribute the observed shift of the proton emission direction in large part to a deformation of the target rear side, induced by the shock wave from the controlled pre-pulse. This deformation alters the sheath field geometry at the time of the main pulse arrival, as also supported by FLASH-2D hydrodynamic simulations.

However, the underlying laser–plasma interaction is complex and may involve additional effects beyond rear-side deformation, such as variations in electron acceleration, local changes in laser energy deposition, self-focusing, or reflection angle. A complete disentangling of these contributions would require additional targeted diagnostics or advanced 3D PIC modeling, which are beyond the scope of this work. Nevertheless, the experimental trends and hydrodynamic simulations suggest that rear-side deformation is a dominant factor in the directional shift observed.

Figure 8 shows the simulated electron density distributions from FLASH-2D simulations for a 1 ns pre-pulse at a 0.5 ns delay. To compare with experimental configuration, the simulation box was rotated by 25°, corresponding to the angle between the laser axis and target normal in the experiment. In this rotated frame, the initial target surface of the undeformed target aligns with 25° (black dotted line). However, when a pre-pulse is introduced, the shock-driven target deformation modifies this geometry. In the 0.5 ns delay case, the shock-driven expansion of the target rear side leads to a deformation that tilts the effective target normal direction to 14.6°, closer to the laser axis. Moreover, the FLASH simulations capture the general trend of ion beam deflection via the evolving target shape. While the simulated deformation progresses are slower compared to the experiment,

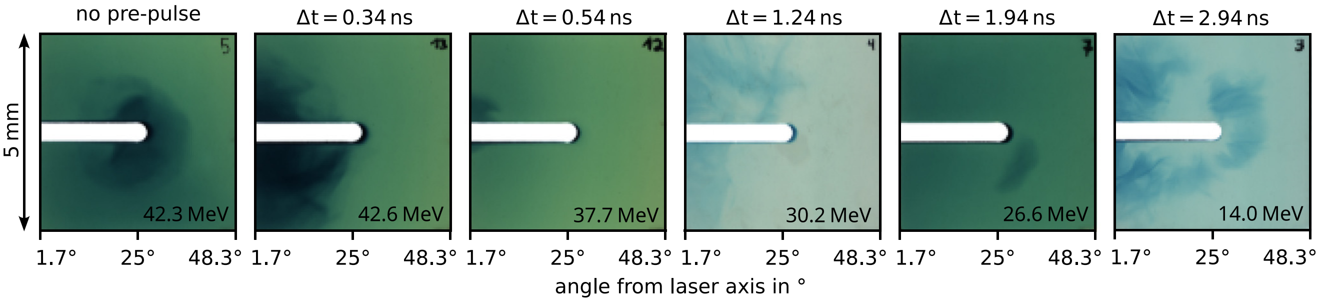

FIG. 7. RCFs of the last layer for each shot, corresponding to the highest measured proton energy. The RCF stack was positioned parallel to the target surface. Thus, the left side corresponds to an emission angle of 1.7°, the center to 25° (target normal), and the right side to 48.3° relative to the laser propagation axis.

TABLE I. Overview of laser parameters, focal spot sizes, and measured/simulated scale lengths for each shot. For the scale lengths at $n_e = 10^{19}\,\mathrm{cm}^{-3}$, $3\,\sigma$ uncertainties are given. For the shot with no pre-pulse, the pre-plasma expansion could not be resolved and thus no scale length measured. The simulated scale length in this case was determined based on a hydro simulation with the rising slope of the laser.

Pre-pulse delay Δt in ns	Laser energy on target E_{laser} in J	Main pulse spot size $\mathrm{FWHM}_{\mathrm{main}}$ in μm	Pre-pulse spot size $\mathrm{FWHM}_{\mathrm{pre}}$ in μm	Measured scale length L_n^{exp} in μm	Simulated scale length L_n^{sim} in μm
No pre-pulse	95.89	2.66 ± 0.17	⋯	⋯	4.36 ± 0.79
0.34 ± 0.17	120.01	2.78 ± 0.24	8.27 ± 0.58	26.92 ± 1.23	35.53 ± 3.74
0.54 ± 0.17	82.80	2.78 ± 0.25	8.27 ± 0.40	39.38 ± 1.16	45.20 ± 6.90
1.24 ± 0.16	96.92	2.76 ± 0.19	8.26 ± 0.55	109.88 ± 39.19	70.00 ± 16.77
1.94 ± 0.16	105.60	2.54 ± 0.12	8.14 ± 0.39	80.37 ± 12.85	96.78 ± 5.15
2.94 ± 0.16	102.65	2.79 ± 0.18	8.34 ± 0.46	83.10 ± 14.67	90.31 ± 12.17

the effective normal direction approaches 0° around 0.9 ns, indicating a clear shift toward the laser axis over time.

The pre-pulse-induced deformation alters the sheath field topology, redirecting ion acceleration toward the laser axis. This effect is particularly relevant for other high-intensity laser facilities, where high Amplified Spontaneous Emission (ASE) levels may induce comparable pre-plasma effects. Therefore, careful consideration of pre-pulse conditions is essential when identifying acceleration regimes and optimizing experimental parameters.

VI. DISCUSSION AND CONCLUSION

In this study, we investigated the influence of pre-plasma formation on ion acceleration in the TNSA regime through a combination of an experiment and hydrodynamic simulations. The experiment was conducted at the PHELIX facility, where we systematically varied the pre-pulse delay and analyzed the resulting pre-plasma and ion beam dynamics using side-view interferometry, TP spectrometers, and RCF diagnostics. Hydrodynamic simulations with FLASH-2D were adapted to match the experimental interferometric measurements, providing deeper insights into the evolution of the pre-plasma.

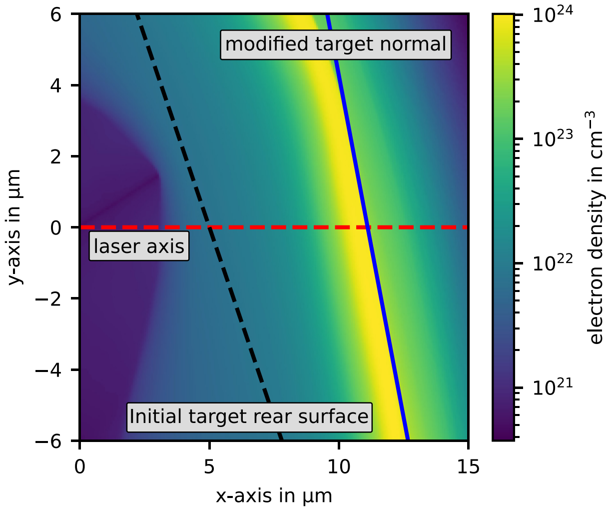

FIG. 8. Electron density distributions from FLASH-2D simulations with a 1 ns pre-pulse at a 0.5 ns delay. Target deformation leads to a tilt of the effective normal direction from 25° (black dotted line) to 14.6° (blue line). The red dotted line shows the actual laser axis after target rotation.

Our results demonstrate that pre-pulse-induced target deformation significantly affects both ion energy cutoffs and ion beam directionality. The presence of a pre-pulse led to a systematic reduction in maximum ion energies, which we attribute to target rear-side expansion and a subsequent decrease in the accelerating sheath field strength. Additionally, ion beam deflection was observed experimentally. The ion beam consistently shifted away from the initial target normal direction toward the laser propagation axis, correlating with a tilting of the effective target normal due to shock-driven deformation.

While previous studies have established that pre-plasma conditions influence the efficiency of laser-ion acceleration, our findings highlight the critical role of target deformation in modifying acceleration geometries. Unlike experiments relying on ASE levels, our controlled pre-pulse approach enabled systematic variation of pre-plasma conditions, establishing a clear correlation between pre-pulse parameters and ion beam deflection. This complements previous work, such as Batani *et al.*,[19] who also observed pre-pulse-induced ion beam deviation but under different laser and target conditions. By integrating hydrodynamic simulations, we extend the understanding of these effects beyond experimental observations and provide a predictive framework for pre-plasma evolution.

These results highlight the importance of carefully controlling pre-pulse conditions in high-intensity laser-plasma experiments. The ability to manipulate ion beam trajectories through controlled pre-pulse-induced deformation could be utilized for beam steering applications or tailored acceleration setups. At the same time, our findings emphasize the necessity of distinguishing between actual changes in the acceleration mechanism and modifications induced by pre-plasma effects. Ion beam deflection, as observed in our study, does not indicate a transition to an alternative acceleration regime but is instead a direct consequence of target deformation affecting the sheath field topology.

While having an independent control over the pre-pulse is a great advantage, one of the limitation met during the experiment has been the relative jitter around 0.3 ns (peak-to-valley) between the pre- and main pulses, due to the generation process of the two independent lasers used in the front end at PHELIX. This has prevented us from studying pre-pulse effects occurring at delays of only tens of picoseconds. In the future, an improved relative timing at PHELIX will enable working with thinner targets, below 1 μm, where the effect of the pre-pulse could be more dramatic.

In any case, our results serve as a cautionary note for experiments investigating alternative ion acceleration mechanisms, such as Radiation Pressure Acceleration (RPA). In such regimes, the presence of pre-plasma can significantly alter target properties, potentially suppressing the acceleration process or leading to misinterpretations of the underlying physics. This underscores the need for precise diagnostics and careful experimental design when studying laser-driven ion acceleration.

ACKNOWLEDGMENTS

The presented experimental results are based on the experiment P-21-00008, which was performed at the target station PTA at the PHELIX laser facility at the GSI Helmholtzzentrum für Schwerionenforschung, Darmstadt (Germany) in the frame of FAIR Phase-0. This work has received funding by the European Union via the Euratom Research and Training Programme (Grant Agreement No. 101052200-EUROfusion). This does not alter the author(s)' adherence to objectivity in presenting the results. Views and opinions expressed are those of the author(s) only and do not necessarily reflect those of the European Union or the European Commission. Neither the European Union not the European Commission can be held responsible for them. The software FLASH code used in this work was developed in part by the DOE NNSA- and DOE Office of Science-supported Flash Center for Computational Science at the University of Chicago and the University of Rochester. This research was supported in part by the cluster computing resource provided by the IT Department at the GSI Helmholtzzentrum für Schwerionenforschung, Darmstadt, Germany. This work was supported by Project ELI-RO/DFG/2023_001 ARNPhot funded by Institute of Atomic Physics Romania. The authors would like to address special thanks to the target laboratory group at GSI under the management of B. Lommel for the production of the carbon targets. Special thanks also go to the PHELIX group for their contributed to the success of the beamtime.

AUTHOR DECLARATIONS

Conflict of Interest

The authors have no conflicts to disclose.

Author Contributions

P. Boller: Conceptualization (equal); Formal analysis (lead); Investigation (lead); Methodology (lead); Project administration (equal); Software (lead); Validation (lead); Visualization (lead); Writing – original draft (lead); Writing – review and editing (equal). **J. Hornung:** Conceptualization (equal); Project administration (equal); Software (supporting); Supervision (lead); Validation (equal); Writing – review and editing (equal). **A. Dumitru:** Investigation (supporting). **C. Kanstein:** Investigation (supporting); Writing – review & editing (supporting). **E. Oezalp:** Investigation (supporting). **J. B. Ohland:** Investigation (supporting); Writing – review and editing (supporting). **L. Wegert:** Formal analysis (supporting); Software (supporting); Writing – review and editing (supporting). **V. Bagnoud:** Conceptualization (equal); Project administration (equal); Supervision (equal); Validation (equal); Writing – review and editing (equal).

DATA AVAILABILITY

The data that support the findings of this study are openlyavailable from Zenodo at DOI: 10.5281/zenodo.16631505.

REFERENCES

[1] M. Aléonard, M. Altarelli, P. Antici, A. Apolonskiy, P. Audebert, A. Bartnik, C. Barty, A. Bernstein, J. Biegert, P. Böni, N. Booth, D. Bote, S. Bulanov, R. Butkus, L. Cardoso, J. Chambaret, D. Charambilidis, G. Cheriaux, R. Clarke, and M. Zepf, *WHITEBOOK ELI – Extreme Light Infrastructure; Science and Technology with Ultra-Intense Lasers* (Andreas Thoss, 2011).

[2] J. Badziak, "Laser-driven ion acceleration: Methods, challenges and prospects," J. Phys.: Conf. Ser. **959**, 012001 (2018).

[3] S. Gales, K. Tanaka, D. Balabanski, F. Negoita, D. Stutman, O. Tesileanu, C. Ur, D. Ursescu, I. Andrei, S. Ataman *et al.*, "The extreme light infrastructure—nuclear physics (ELI-NP) facility: New horizons in physics with 10 PW ultra-intense lasers and 20 MeV brilliant gamma beams," Rep. Prog. Phys. **81**, 094301 (2018).

[4] L. Kiani, T. Zhou, S.-W. Bahk, J. Bromage, D. Bruhwiler, E. M. Campbell, Z. Chang, E. Chowdhury, M. Downer, Q. Du *et al.*, "High average power ultrafast laser technologies for driving future advanced accelerators," J. Instrum. **18**, T08006 (2023).

[5] A. Macchi, M. Borghesi, and M. Passoni, "Ion acceleration by superintense laser-plasma interaction," Rev. Mod. Phys. **85**, 751–793 (2013).

[6] H. Daido, M. Nishiuchi, and A. S. Pirozhkov, "Review of laser-driven ion sources and their applications," Rep. Prog. Phys. **75**, 056401 (2012).

[7] J. Fuchs, P. Audebert, M. Borghesi, H. Pépin, and O. Willi, "Laser acceleration of low emittance, high energy ions and applications," C. R. Phys. **10**, 176–187 (2009).

[8] S. V. Bulanov, J. J. Wilkens, T. Z. Esirkepov, G. Korn, G. Kraft, S. D. Kraft, M. Molls, and V. S. Khoroshkov, "Laser ion acceleration for hadron therapy," Phys.-Usp. **57**, 1149 (2014).

[9] M. Passoni, F. Arioli, L. Cialfi, D. Dellasega, L. Fedeli, A. Formenti, A. C. Giovannelli, A. Maffini, F. Mirani, A. Pazzaglia *et al.*, "Advanced laser-driven ion sources and their applications in materials and nuclear science," Plasma Phys. Controlled Fusion **62**, 014022 (2020).

[10] E. Esarey, C. B. Schroeder, and W. P. Leemans, "Physics of laser-driven plasma-based electron accelerators," Rev. Mod. Phys. **81**, 1229–1285 (2009).

[11] A. Maffini, F. Mirani, M. Galbiati, K. Ambrogioni, F. Gatti, M. S. G. De Magistris, D. Vavassori, D. Orecchia, D. Dellasega, V. Russo *et al.*, "Towards compact laser-driven accelerators: Exploring the potential of advanced double-layer targets," EPJ Tech. Instrum. **10**, 15 (2023).

[12] A. Higginson, R. Gray, M. King, R. Dance, S. Williamson, N. Butler, R. Wilson, R. Capdessus, C. Armstrong, J. Green *et al.*, "Near-100 MeV protons via a laser-driven transparency-enhanced hybrid acceleration scheme," Nat. Commun. **9**, 724 (2018).

[13] N. P. Dover, T. Ziegler, S. Assenbaum, C. Bernert, S. Bock, F.-E. Brack, T. E. Cowan, E. J. Ditter, M. Garten, L. Gaus *et al.*, "Enhanced ion acceleration from transparency-driven foils demonstrated at two ultraintense laser facilities," Light: Sci. Appl. **12**, 71 (2023).

[14] T. Ziegler, I. Göthel, S. Assenbaum, C. Bernert, F.-E. Brack, T. E. Cowan, N. P. Dover, L. Gaus, T. Kluge, S. Kraft *et al.*, "Laser-driven high-energy proton beams from cascaded acceleration regimes," Nat. Phys. **20**, 1211–1216 (2024).

[15] R. Snavely, M. Key, S. Hatchett, T. Cowan, M. Roth, T. Phillips, M. Stoyer, E. Henry, T. Sangster, M. Singh *et al.*, "Intense high-energy proton beams from petawatt-laser irradiation of solids," Phys. Rev. Lett. **85**, 2945 (2000).

[16] S. P. Hatchett, C. G. Brown, T. E. Cowan, E. A. Henry, J. S. Johnson, M. H. Key, J. A. Koch, A. B. Langdon, B. F. Lasinski, R. W. Lee *et al.*, "Electron, photon, and ion beams from the relativistic interaction of petawatt laser pulses with solid targets," Phys. Plasmas **7**, 2076–2082 (2000).

[17] S. Wilks, A. Langdon, T. Cowan, M. Roth, M. Singh, S. Hatchett, M. Key, D. Pennington, A. MacKinnon, and R. Snavely, "Energetic proton generation in ultra-intense laser–solid interactions," Phys. Plasmas **8**, 542–549 (2001).

[18] J. Hornung, Y. Zobus, P. Boller, C. Brabetz, U. Eisenbarth, T. Kühl, Z. Major, J. Ohland, M. Zepf, B. Zielbauer *et al.*, "Enhancement of the laser-driven proton source at PHELIX," High Power Laser Sci. Eng. **8**, e24 (2020).

[19] D. Batani, R. Jafer, M. Veltcheva, R. Dezulian, O. Lundh, F. Lindau, A. Persson, K. Osvay, C. Wahlström, D. Carroll *et al.*, "Effects of laser prepulses on laser-induced proton generation," New J. Phys. **12**, 045018 (2010).

[20] J. Fuchs, P. Antici, E. d'Humieres, E. Lefebvre, M. Borghesi, E. Brambrink, C. Cecchetti, M. Kaluza, V. Malka, M. Manclossi *et al.*, "Laser-driven proton scaling laws and new paths towards energy increase," Nat. Phys. **2**, 48–54 (2006).

[21] M. Kaluza, J. Schreiber, M. I. Santala, G. D. Tsakiris, K. Eidmann, J. Meyer-ter Vehn, and K. J. Witte, "Influence of the laser prepulse on proton acceleration in thin-foil experiments," Phys. Rev. Lett. **93**, 045003 (2004).

[22] F. Zheng, S. Wu, H. Zhang, T. Huang, M. Yu, C. Zhou, and X. He, "Preplasma effects on the generation of high-energy protons in ultraintense laser interaction with foil targets," Phys. Plasmas **20**, 123105 (2013).

[23] P. Hadjisolomou, I. Tsygvintsev, P. Sasorov, V. Gasilov, G. Korn, and S. Bulanov, "Preplasma effects on laser ion generation from thin foil targets," Phys. Plasmas **27**, 013107 (2020).

[24] A. Yogo, H. Daido, S. Bulanov, K. Nemoto, Y. Oishi, T. Nayuki, T. Fujii, K. Ogura, S. Orimo, A. Sagisaka *et al.*, "Laser ion acceleration via control of the near-critical density target," Phys. Rev. E **77**, 016401 (2008).

[25] A. Flacco, A. Guemnie-Tafo, R. Nuter, M. Veltcheva, D. Batani, E. Lefebvre, and V. Malka, "Characterization of a controlled plasma expansion in vacuum for laser driven ion acceleration," J. Appl. Phys. **104**, 103304 (2008).

[26] Z. Major, U. Eisenbarth, B. Zielbauer, C. Brabetz, J. Ohland, Y. Zobus, S. Roeder, D. Reemts, S. Kunzer, S. Götte *et al.*, "High-energy laser facility PHELIX at GSI: Latest advances and extended capabilities," High Power Laser Sci. Eng. **12**, e39 (2024).

[27] B. Fryxell, K. Olson, P. Ricker, F. X. Timmes, M. Zingale, D. Lamb, P. MacNeice, R. Rosner, J. Truran, and H. Tufo, "FLASH: An adaptive mesh hydrodynamics code for modelingastrophysical thermonuclear flashes," Astrophys. J., Suppl. Ser. **131**, 273 (2000).

[28] J. Ohland, U. Eisenbarth, B. Zielbauer, Y. Zobus, D. Posor, J. Hornung, D. Reemts, and V. Bagnoud, "Ultra-compact post-compressor on-shot wavefront measurement for beam correction at PHELIX," High Power Laser Sci. Eng. **10**, e18 (2022).

[29] B. Kindler, W. Hartmann, J. Klemm, B. Lommel, and J. Steiner, "Preparation of targets by sputter deposition," Nucl. Instrum. Methods Phys. Res., Sect. A **521**, 222–226 (2004).

[30] J. Hornung, Y. Zobus, H. Lorenté, C. Brabetz, B. Zielbauer, and V. Bagnoud, "Synchronized off-harmonic probe laser with highly variable pulse duration for laser–plasma interaction experiments," High Power Laser Sci. Eng. **12**, e10 (2024).

[31] D. Carroll, P. Brummitt, D. Neely, F. Lindau, O. Lundh, C.-G. Wahlström, and P. McKenna, "A modified Thomson parabola spectrometer for high resolution multi-MeV ion measurements—Application to laser-driven ion acceleration," Nucl. Instrum. Methods Phys. Res., Sect. A **620**, 23–27 (2010).

[32] D. Descamps, C. Lyngå, J. Norin, A. L'Huillier, C.-G. Wahlström, J.-F. Hergott, H. Merdji, P. Salières, M. Bellini, and T. Hänsch, "Extreme ultraviolet interferometry measurements with high-order harmonics," Opt. Lett. **25**, 135–137 (2000).

[33] A. Aliverdiev, D. Batani, R. Dezulian, T. Vinci, A. Benuzzi-Mounaix, M. Koenig, and V. Malka, "Hydrodynamics of laser-produced plasma corona measured by optical interferometry," Plasma Phys. Controlled Fusion **50**, 105013 (2008).

[34] N. Meezan, R. Berger, L. Divol, D. Froula, D. Hinkel, O. Jones, R. London, J. Moody, M. Marinak, C. Niemann *et al.*, "Role of hydrodynamics simulations in laser-plasma interaction predictive capability," Phys. Plasmas **14**, 056304 (2007).

[35] C. Orban, M. Fatenejad, and D. Q. Lamb, "Code-to-code comparison and validation of the radiation-hydrodynamics capabilities of the flash code using a laboratory astrophysical jet," Phys. Plasmas **29**, 053901 (2022).

[36] S. Weber, G. Riazuelo, P. Michel, R. Loubere, F. Walraet, V. Tikhonchuk, V. Malka, J. Ovadia, and G. Bonnaud, "Modeling laser–plasma interaction hydrodynamic scales: Phys. development comparison with experiments," Laser Part. Beams **22**, 189–195 (2004).

[37] J. Limpouch, V. Tikhonchuk, O. Renner, S. Agarwal, T. Burian, J. Červenka, J. Dostál, R. Dudžák, D. Ettel, A. Gintrand *et al.*, "Laser interaction with undercritical foams of different spatial structures," Matter Radiat. Extremes **10**, 017402 (2025).

[38] Los Alamos National Laboratory, "SESAME: The Los Alamos National Laboratory equation of state database," Technical Report No. LA-UR-92-407, Los Alamos National Laboratory, 1979.

[39] N. H. Magee, J. Abdallah, R. E. H. Clark, J. S. Cohen, L. A. Collins, G. Csanak, C. J. Fontes, A. Gauger, J. J. Keady, D. P. Kilcrease, and A. L. Merts, "Atomic structure calculations and new Los Alamos astrophysical opacities," in *Astrophysical Applications of Powerful New Databases*, edited by S. J. Adelman and W. L. Wiese (Astronomical Society of the Pacific, 1995), Vol. 78, p. 51.

[40] K. Zeil, S. Kraft, S. Bock, M. Bussmann, T. Cowan, T. Kluge, J. Metzkes, T. Richter, R. Sauerbrey, and U. Schramm, "The scaling of proton energies in ultrashort pulse laser plasma acceleration," New J. Phys. **12**, 045015 (2010).

[41] M. Zimmer, S. Scheuren, T. Ebert, G. Schaumann, B. Schmitz, J. Hornung, V. Bagnoud, C. Rödel, and M. Roth, "Analysis of laser-proton acceleration experiments for development of empirical scaling laws," Phys. Rev. E **104**, 045210 (2021).

[42] S. Keppler, N. Elkina, G. Becker, J. Hein, M. Hornung, M. Mäusezahl, C. Rödel, I. Tamer, M. Zepf, and M. Kaluza, "Intensity scaling limitations of laser-driven proton acceleration in the TNSA-regime," Phys. Rev. Res. **4**, 013065 (2022).